

REPORT DOCUMENTATION PAGE				
1a. REPORT SECURITY CLASSIFICATION <b>UNCLASSIFIED</b>		1b. RESTRICTIVE MARKINGS		
2a. SECURITY CLASSIFICATION AUTHORITY		3. DISTRIBUTION / AVAILABILITY OF REPORT  Approved for public release; distribution unlimited.		
2b. DECLASSIFICATION / DOWNGRADING SCHEDULE				
4. PERFORMING ORGANIZATION REPORT NUMBER(S)  NRL Memorandum Report 5479		5. MONITORING ORGANIZATION REPORT NUMBER(S)		
6a. NAME OF PERFORMING ORGANIZATION  Naval Research Laboratory	6b. OFFICE SYMBOL (If applicable)  Code 5310	7a. NAME OF MONITORING ORGANIZATION		
6c. ADDRESS (City, State, and ZIP Code)  Washington, DC 20375-5000		7b. ADDRESS (City, State, and ZIP Code)		
8a. NAME OF FUNDING / SPONSORING ORGANIZATION  Office of Naval Research	8b. OFFICE SYMBOL (If applicable)	9. PROCUREMENT INSTRUMENT IDENTIFICATION NUMBER		
8c. ADDRESS (City, State, and ZIP Code)  Arlington, VA 22217		10. SOURCE OF FUNDING NUMBERS		
		PROGRAM ELEMENT NO.  61153N	PROJECT NO.	TASK NO. RR021-  05-41
				WORK UNIT ACCESSION NO.  DN480-006
11. TITLE (Include Security Classification)  Experimental Test of the Three Subaperture Method for Estimating Target Elevation Angle				
12. PERSONAL AUTHOR(S)  Gordon, W.B.				
13a. TYPE OF REPORT  Interim	13b. TIME COVERED FROM 10/82 TO 9/83	14. DATE OF REPORT (Year, Month, Day)  1984 December 31	15. PAGE COUNT  33	
16. SUPPLEMENTARY NOTATION				
17. COSATI CODES			18. SUBJECT TERMS (Continue on reverse if necessary and identify by block number)  Elevation angle estimation                      Three subaperture method Non-linear spectral estimation	
FIELD	GROUP	SUB-GROUP		
19. ABSTRACT (Continue on reverse if necessary and identify by block number)  Experimental radar measurements were taken on a target aircraft flying low over a smooth reflecting sea for the purpose of testing the three subaperture method, which is a non-linear technique for estimating the elevation angle of a target in the presence of multipath. The experimental array employed three vertically mounted dishes and three receivers, and the system stability proved to be more than adequate to permit interchannel gain and phase calibrations to be made by an appropriate numerical processing of the data. The standard deviations of the angle estimates were found to conform to theoretical expectations, but the biases were often large and exhibited a certain peculiar degeneracy in the vicinity of multipath nulls; viz., a sharp and rapid increase as the target approached a null followed by an abrupt change in sign as the target emerged from the null. Computer simulations were used to determine whether this peculiar "angle flip-flop" phenomenon could have been caused by (1) refractive ray bending, (2) uncompensated array tilt, (3) diffuse  (Continues)				
20. DISTRIBUTION / AVAILABILITY OF ABSTRACT <input checked="" type="checkbox"/> UNCLASSIFIED/UNLIMITED <input type="checkbox"/> SAME AS RPT <input type="checkbox"/> DTIC USERS		21. ABSTRACT SECURITY CLASSIFICATION  <b>UNCLASSIFIED</b>		
22a. NAME OF RESPONSIBLE INDIVIDUAL  W. B. Gordon		22b. TELEPHONE (Include Area Code)  (202) 767-2399	22c. OFFICE SYMBOL  Code 5310	

19. ABSTRACT (Continued)

scattering from the sea surface, or by (4) diffraction of the echo signal around obstacles located in the near vicinity of the radar. It was found that although the first two mechanisms can produce large biases, such biases are symmetric about the multipath nulls, whereas the latter two mechanisms can produce biases which are both large and skew-symmetric about the nulls. We therefore conclude that one of the latter two mechanisms was responsible for the observed large biases.

# Experimental Test of the Three Subaperture Method for Estimating Target Elevation Angle

W. B. GORDON

*Radar Analysis Branch  
Radar Division*

December 31, 1984



NAVAL RESEARCH LABORATORY,  
Washington, D.C.

## CONTENTS

1. INTRODUCTION .....	1
2. SYSTEM CALIBRATION .....	3
3. ANALYSIS OF THE EXPERIMENTAL RESULTS .....	3
A. Calibration Errors .....	4
B. Statistical Errors .....	4
C. Model Errors .....	6
4. SUMMARY, CONCLUSIONS, AND RECOMMENDATIONS .....	10
5. REFERENCES .....	24
APPENDIX A: THE THREE SUBAPERTURE ALGORITHM .....	25
APPENDIX B: SYSTEM ASYMMETRIES .....	27

EXPERIMENTAL TEST OF THE THREE SUBAPERTURE METHOD FOR  
ESTIMATING TARGET ELEVATION ANGLE

1. INTRODUCTION

Non-linear techniques in spectral analysis is an active area of current research with potential applications to antenna processing, and in recent years workers at NRL have investigated the possibility of using such techniques for measuring the elevation angle of radar targets located above a smooth reflecting sea [1, 2, 3, 4]. Several algorithms have been devised whose salient features are the following:

(1) The algorithms use the outputs of three subapertures as inputs to the angle estimators, and hence only three receivers are required to implement the scheme.

(2) The angle estimates are in closed form, and easy to implement numerically since they only require the solution of a 2 by 2 system of linear equations and the extraction of roots.

(3) The solutions are exact when noise is absent and the target's multipath image (reflected off the sea) consists of a single specular component.

(4) In the presence of noise the accuracy of the algorithms is comparable to that of the maximum likelihood estimator, which is known to be optimal or close to optimal [3, 4, 5, 6].

In this report we shall describe the results of field tests with an experimental L-band system whose parameters are shown in Table 1. The experimental receive array uses three dishes to mimic the effect of three subapertures, and lies 30 m above the water surface. A separate radar located behind and 2 m above the receive array is used to illuminate the target and record range data. An optical tracker is used to steer the transmitter dish and record elevation angle data. The test site is located at the Randle Cliff facility on the Western Shore of the Chesapeake Bay, and the target aircraft was an Orion P3 which flew straight line courses at a constant height above the Bay. A CW transmitter located at the Tilghman Island site on the Eastern Shore was used for system calibration. The data from three different days (5 March, 17 May, and 9 September 1982) was used in the preparation of this report.

The output from each dish is fed to a separate mixer where the I- and Q-channel voltages are extracted, and then recorded on magnetic tape for subsequent processing. Hence each radar pulse produces six quantities (the

Manuscript approved August 15, 1984.

TABLE 1

## System Parameters

Frequency	1.3 GHz
Polarization	Horizontal
Prf	500 Hz
Bandwidth	1.0 MHz
Transmitter Beamwidth	6.0°
Receive Array Beamwidths	
Elevation	4.4°
Azimuth	13.3°
Height of Transmitter Dish	31.85 m
Height of Receive Array	30.0 m

three pairs of I- and Q-voltages), which are used as inputs to algorithms which extract estimates of six other quantities, viz., the elevation angles, amplitudes, and phases of the target and its multipath image. A basic assumption in deriving the algorithms is the absence of diffuse scattering components, so that the received signal is indeed characterized by these six quantities. The algorithms are discussed in detail in References [3] and [4], but for purposes of reference the equations used for angle estimation are repeated here in Appendix A.

In References [3] and [4] we also describe the results of computer simulations used to calculate the rms errors as a function of the free space signal-to-noise power ratio  $S/N$ , the relative phase  $\phi$  between the direct and reflected ray, and the magnitude  $\rho$  of the reflection coefficient.

The experimental results will be presented in Section 3. It turned out that the signal-to-noise ratio was only infrequently as large as we would have desired, and the analysis of the data was made difficult by a large and rapid signal modulation (20 dB at 15 Hz) which was apparently produced by aircraft wobble and prop motion. In comparing the experimental angle measurement errors with those predicted by theory, we found that the standard deviations of the angle estimates fell within the predicted range but that the biases were larger than expected and behaved in a peculiar way (to be described) as the target approached a multipath null. There are four possible mechanisms which might explain the large biases: (1) refractive bending of the rays, (2) small asymmetries between the direct and reflected rays around the radar line-of-sight which were not properly accounted for in the algorithm, and (3) diffuse scattering from the sea surface, and (4) diffraction of the echo signal around obstacles located in the near field of the receive array. Computer simulations were used to calculate the effects of these mechanisms, and for reasons to be explained in Section 3, it appears that only the third and fourth possibilities can account for the observed phenomena. Finally, we note that the data were taken on days of flat calm or very light winds so that, in terms of sea smoothness, the conditions were near optimal for simple specular reflection from the sea surface.

## 2. SYSTEM CALIBRATION

The receive array is mounted on a frame that can be manually rotated about the array axis, and during the first set of calibration measurements the three dishes were horizontally aligned and pointed at the CW transmitter on Tilghman Island. These recordings were used to calculate the bias voltages and gains in each of the channels and the cross correlations between the I- and Q-channel voltages from each receiver. These biases and cross correlations were then removed by subsequent computer processing, and the relative gains were adjusted to unity.

The turnstile on which the frame is mounted was then mechanically steered through an arc of  $\pm 45^\circ$  about the Tilghman Island source. A plot of instantaneous power ( $= I^2 + Q^2$ ) from one of the dishes is shown in Figure 1. The antenna patterns thus obtained were smoothed and beam split to determine the location of the three beam centers, (which were found to be virtually the same for all dishes). The relative phases  $\varphi_{21}$  and  $\varphi_{23}$  between the middle dish (taken as the reference) and the two end dishes are also calculated from the data taken as the array swings past the source, and a typical example of a plot thus obtained is shown in Figure 2. For a perfectly calibrated system, the intersection of the two lines in the phase plot should intersect at a position corresponding to the beam center. The two lines were smoothed and the calculated value of the beam center was used to estimate the actual phase errors. Figure 3 shows the results for 12 phase error measurements taken over a one hour time span, consisting of four groups of three closely spaced measurements. Also shown are phase error measurements taken from an internal pilot signal which was designed to be used for this purpose. We therefore had available two independent measurements of phase error which were used in the subsequent computer processing, even though they were found to have only a very small effect on the elevation angle estimate.

The final step in the calibration process consisted of turning off the CW transmitter and taking measurements of the receiver noise. These noise values were used to compare the actual error curves with those obtained by the computer simulations discussed in [3,4].

Calibration measurements were always taken before the arrival of the P3 at the test site and immediately after its departure at the conclusion of the elevation angle radar measurements. After the initial set of calibration measurements, the array had to be manually rotated to a vertical position before taking the elevation angle radar measurements. It was originally intended to take calibration measurements at intervals during the radar measurements; however, this proved to be impractical because of the necessity of rotating the array, and also unnecessary since the system drift was found to be slow and had a very small effect on the angle measurements.

## 3. ANALYSIS OF THE EXPERIMENTAL RESULTS

It will be convenient to discuss the experimental results from the standpoint of the various types of errors that can affect the measurement process.

A. Calibration Errors. To gauge the effects of possible errors in the system calibration (discussed in the previous section), as an experiment the calibration adjustments in the numerical processing were first deleted and then enhanced (within reasonable limits). For example, in one calculation we actually reversed the signs of the inter-channel phase adjustments. Although the effects of such deliberate sabotage were usually discernible, they were much too small to explain the discrepancies between the experimental results and theoretical predictions discussed below.

B. Statistical Errors. The statistical error is the unavoidable error produced by receiver noise. It is a function of the free space signal-to-noise power ratio (S/N) (integrated over the entire aperture), the relative phase  $\varphi$  between the direct and reflected rays (measured at the center of the aperture), the magnitude  $\rho$  of the reflection coefficient, and the elevation angle  $\theta$ . Computer simulations were used to examine the functional dependence of the statistical error on these parameters, and the results are discussed in [3]. Our analysis of the actual error curves (derived from the data) was made extremely difficult by rapid fluctuations in the signal power and variations in phase which in turn made it hard to isolate the effects of the various parameters on the algorithm performance.

Figures 4-9 show the results from 6 consecutive data files taken during a run during which the P3 was flying inbound (towards the test site) at a height of 354 m at a speed of approximately 111 m/s. (Due to the presence of heavy fog this was twice the desired height originally requested.) In each figure the top trace is a plot of the instantaneous power ( $I^2 + Q^2$ ) at the center dish (in dB), and the middle and lower plots show two outputs from the algorithm, viz., the estimated values of  $\theta$  and  $\varphi$ . (The plots for the corresponding values of  $\rho$  have no particular interest and are not shown. The data was consistent with a value  $\rho \approx 0.9$ .) Each file consists of slightly more than 4 seconds of data taken at a prf of 500 Hz. There was a 2 second delay between consecutive files, which was required to dump the data from a minicomputer into mag tape. The horizontal (time) axes are labelled with pulse numbers in increments of 400, and the data is quantized along the horizontal axes, so that each plot consists of 100 vertical lines, each of which depict the data from 20 consecutive pulses.

The power plots typically show a 20 dB variation every 20-40 pulses (i.e., over one or two consecutive vertical lines). One obvious source for this rapid modulation is the aircraft prop motion. The Orion P-3 has a turbo prop engine and its four bladed props rotate at a constant shaft speed of 1020 rpm (17 Hz). Power spectra of the target echo were calculated, and were usually found to contain a spike near a frequency (68 Hz) equal to four times the shaft speed. The power spectra also had a number of spikes between 1 and 5 Hz which were sometimes larger than the spike at 68 Hz, and were apparently caused by aircraft wobble. This rapid 20 dB variation in signal power is responsible for much of the jitter shown in the plots for  $\theta$  and  $\varphi$ .

In addition to the rapid signal modulation caused by prop motion and aircraft wobble, there is a slower modulation produced by multipath effects, which are clearly seen by examining the upper and lower envelopes of the power plots in Figures 4-9. This modulation becomes more rapid and the

occurrence of nulls more frequent as the range decreases. We recall that the transmit and receive antennas are not colocated so that the multipath transmit and receive nulls are not necessarily coincident (except at large ranges). In principle, the receive nulls can be distinguished from the transmit nulls since the former occur only when  $\varphi = 180^\circ$ . Thus, for example, files 85 and 88 both appear to be emerging from a null at their beginnings, but by examining the corresponding phase plots it appears that only the latter is a receive null. Similarly, it seems clear that the nulls in files 89 and 90 are also receive nulls.

The free space signal-to-noise power ratio  $S/N$  is by definition the signal-to-noise ratio that would occur in the absence of a reflecting sea; it is not a direct observable, but must be calculated as a function of  $\varphi$ ,  $\rho$ , and the actual signal power. For example, in files 88-90 where the nulls are clearly receive nulls ( $\varphi = 180^\circ$ ), the actual signal power maximum (as seen in the upper or lower envelope) occurs when  $\varphi = 0^\circ$ , as one would expect. Assuming  $\rho = .9$ , and from the measured values of the noise parameters, one can determine that  $S/N$  is 14 dB less than the actual signal power at the peak locations, but at these locations only. For example, in file 89 the peak value of the upper envelope is 60 dB and about 40 dB at the lower one. Hence  $S/N$  varies between 26 dB and 46 dB near the peak. However, due to the effects of the transmitter multipath, it is not necessarily the case that  $S/N$  will remain within these limits over the entire file.

The striking behavior of the angle estimates near the multipath nulls will be discussed in the next paragraph, and we shall now conclude this paragraph by showing how the observed standard deviations in the angle estimates conform to theoretical expectations. Figure 10 is a scatter diagram of "normalized" standard deviations vs.  $\theta$ . The dashed lines labelled  $\varphi = 0^\circ$  and  $\varphi = 180^\circ$  represent the lower and upper bounds to the standard deviations which are attained at these values of phase. Computer calculations showed that the standard deviation in the angle estimate varies as  $1/\sqrt{S/N}$  provided  $S/N > 30$  dB and  $\varphi$  does not fall in the range  $135^\circ < \varphi < 225^\circ$ . The normalization consists of multiplying the actual standard deviation of a sample by  $\sqrt{S/N}/\sqrt{1000}$ , to obtain a value that corresponds to the nominal  $S/N$  value of 30 dB. In calculating the standard deviations we cannot use an entire file as the statistical population because the errors are dependent on the phase  $\varphi$ . Therefore, each file was divided into 20 segments of 100 points each, and the standard deviations were calculated for each of the segments. Hence for each file we have 20 values of the standard deviation in  $\theta$ , but in order to save labor in Figure 10 we have plotted only one value for each file, viz., the numerical average of the 20 values.

There are two types of points shown in the figure, crosses and circles. They correspond to data that was taken on two different days. The circles represent data taken on the same day as the data shown in figures 4-9, when the aircraft was flying at a height of 350 m, vs. a height of 165 m for the data represented by the crosses. The data represented by the circles has also been "edited" in the following way. For each segment we calculated the numerical average of the estimated values of  $\varphi$  and  $\rho$ , and these values were used to calculate  $S/N$  for each of the 100 points in the segment.

Those points for which  $S/N < 30$  dB were rejected, and if less than 16 "good" points remain in the segment then the entire segment is rejected. The average values of  $\theta$ ,  $\varphi$  and  $\rho$  are then calculated for the set of surviving points, and the entire segment is rejected if  $\varphi$  falls in the range  $135^\circ \leq \varphi \leq 225^\circ$ . The circles therefore represent the numerical averages of standard deviations of only those segments which survive the editing process.

Only a very small proportion of the data was found to survive the editing process, and almost all of that which did come from the one day (5 March 82) represented by the circles. In Figure 10 we see that some of the crosses fall below the lower bound limit ( $\varphi = 0^\circ$ ). This is due to the fact that the normalization to the nominal value  $S/N = 30$  dB overcompensates at low  $S/N$  ratios because the increase of the standard deviation in  $\theta$  with decreasing values of  $S/N$  is not as rapid as  $1/\sqrt{S/N}$  when  $S/N < 30$  dB. On the other hand, none of the edited data represented by the circles falls below the lower limit line, and only a few of them lie above the limit line  $\varphi = 135^\circ$ , which increases our confidence that the calculated values of  $S/N$  were at least approximately correct.

C. Model Errors. In the derivation of the algorithm it is assumed that the rays propagate in straight lines and that the target image reflected off the sea consists of a single specular component (no diffuse scattering). It is also assumed that the asymmetries between the direct and reflected rays about the radar line-of-sight are known and have been properly compensated for. These asymmetries are discussed in Appendix B. One of them is produced by an array tilt (departure from the true vertical), and the other, termed the "geometrical effect", arises from the fact that the height of the target above the antenna is less than the height of the antenna above the virtual image. The angle estimates shown in Figures 4-9 are "raw" in the sense that no asymmetry correction has been applied. For example, to correct for the geometric effect, the elevation angle estimates shown in Figures 4-9 should be reduced by 9 percent. The "true" values of  $\theta$  derived from the optical tracker are shown in Table 2.

TABLE 2

Optical Values of Elevation Angle

<u>File</u>	<u>El. Angle</u>
85	2.3°
86	2.5
87	2.7
88	3.0
89	3.3
90	3.7

The most striking feature of these angle plots is the way in which the bias often becomes sharply positive as a closing target approaches a multi-

path receive null, and then abruptly negative just after it emerges from the null. (For a receding target the signs of the biases are reversed.) From an examination of all the data (taken on three different days) it was found that this phenomenon was not always most pronounced at high elevation angles  $\theta$  or short ranges (as might be suggested by comparing the results from Files 85-87 with those from Files 88-90). To give this phenomenon a name, we shall call it the "angle flip-flop" effect.

As the target approaches a receive null we also see many occurrences of a certain limiting value,  $\theta = 6.7^\circ$ . The spacing between the array elements is greater than  $\lambda/2$  and hence there are grating lobes. The value  $\theta = 6.7^\circ$  is the ambiguity limit of the array, and this value is obtained as a certain degenerate solution to the maximum likelihood estimator, and the corresponding phase estimate is  $\varphi = 180^\circ$ . Another degenerate solution is  $\theta = 0^\circ$ , for which the corresponding value of  $\varphi$  is also  $180^\circ$ . The probability of obtaining these degenerate solutions is substantial when S/N is small, and a number of them can be seen at the beginning of File 85.

The biases in the angle estimates can be clearly seen in Figure 11, which depicts a moving average of the angle estimates from Files 85-89. Each point on a curve is the numerical average of 101 angle estimates (including 50 before and 50 after the given time point), and the dashed line represents the "true" elevation angle (derived from the optical tracker). The circles represent actual data points and the rest of the curve has been hand drawn. The open circles correspond to points near a receive null ( $135^\circ < \varphi < 225^\circ$ ), and the angle flip-flop effect is clearly evident in the data from Files 88, 89. These curves show biases at the "good" points (filled-in circles) as large as  $1^\circ$ , with larger biases in the vicinity of multipath nulls. These curves are derived from all the (non-edited) data in the files, however the edited data also shows biases as large as  $1^\circ$  at points far removed from the receive nulls.

We shall now discuss how the large observed biases and the angle flip-flop phenomenon might be explained by the breakdown of one or more of the three assumptions listed at the beginning of this paragraph.

(i) Asymmetries. The "geometric effect" (discussed above and in Appendix B) is small and easily compensated for, and computer simulations revealed that it could not produce the large observed biases. On the other hand, large biases can be produced by small tilt angles, as is shown in Tables 3 and 4. Table 3 shows the biases for various values of S/N and  $\varphi$  when  $\theta = 2.2^\circ$  (= half beamwidth), and Table 4 shows the effects of introducing a one half degree uncompensated tilt. Although the biases are numerically large, they are symmetric around the axis  $\varphi = 180^\circ$ , and hence cannot explain the angle flip-flop phenomenon since the latter is anti-symmetric around this axis. It is possible, however, that an uncompensated tilt was present and modified a diffuse scattering effect. We also note that the symmetry of the tilt effect around  $\varphi = 180^\circ$  persists over a wide range of tilts (up to  $4^\circ$ ), which is somewhat remarkable since our computer simulations took due account of the effects of the antenna lobe pattern.

(ii) Refractive Ray Bending. The effect of refractive ray bending would be to make the arrival angles of the direct and reflected rays more positive

TABLE 3

Theoretically Calculated Biases (deg.) for  $\theta = 2.2^\circ$ , Tilt Angle =  $0.0^\circ$ 

S/N Phase	$0^\circ$	$90^\circ$	$135^\circ$	$157.5^\circ$	$180^\circ$	$202.4^\circ$	$225^\circ$	$270^\circ$
30 dB	0	0	0	- .1	.1	- .1	0	0
24 dB	0	0	-.1	- .2	.8	- .2	-.1	0
18 dB	0	-.1	-.2	0	1.1	0	-.2	-.1
12 dB	-.1	-.2	.1	.8	1.2	.7	0	-.2
6 dB	-.1	.2	.8	1.1	1.3	1.0	.8	.1
0 dB	-.7	.9	1.1	1.2	1.3	1.1	1.0	.8

TABLE 4

Theoretically Calculated Biases (deg.) for  $\theta = 2.2^\circ$ , Tilt Angle =  $0.5^\circ$ 

S/N Phase	$0^\circ$	$90^\circ$	$135^\circ$	$157.5^\circ$	$180^\circ$	$202.5^\circ$	$225^\circ$	$270^\circ$
30 dB	-.1	-.3	-1.0	-2.0	2.2	-2.0	-1.0	-.3
24 dB	-.1	-.3	-1.1	-1.8	2.0	-1.8	-1.1	-.3
18 dB	-.1	-.4	-1.0	-1.5	-1.6	-1.5	-1.0	-.4
12 dB	-.2	-.5	-.5	-.4	-.3	-.4	-.6	-.5
6 dB	-.1	.1	.4	.6	.7	.7	.5	.2
0 dB	.6	.8	1.0	1.2	1.2	1.1	1.0	.8

than they would be for straight line propagation. One would therefore expect that refraction would produce an effect similar to that of an uncompensated tilt. In quantitative terms, the change in arrival angle produced by refraction is approximately  $\Delta\theta = (k/2) R$  where  $R$  is the target range and  $-k$  is the gradient of the refractive index. Hence, for  $\Delta\theta = 0.5^\circ$  at  $R = 6000$  m, we get  $k = 2.9 \times 10^{-6} \text{ m}^{-1}$ , which is approximately 20 times the value required for super-refraction ( $1.6 \times 10^{-7} \text{ m}^{-1}$ ). Other factors militating against refractive bending as a significant effect is the large heights of the antenna (30 m) and aircraft ( $> 150$  m), and the fact that the angle flipflop phenomenon was observed on all three of the days on which data was taken (5 March, 17 May, and 9 September 1982).

(iii) Diffuse Scattering. Figure 12 shows the results of a computer simulated run in which diffuse scattering has been crudely modelled by adding a second reflected ray at an arrival angle  $1^\circ$  above that of the original reflected ray. The amplitudes of both reflected components have been reduced by one-half so that the total power in the reflected images remains the same as that in the original specular component. The peak signal power was chosen to match that in Files 88, 89, but for purposes of graphical clarity the signal modulation has been reduced from 20 dB to 1 dB (at a 15 Hz rate). The "true" elevation angle is  $3^\circ$ , the simulated target's height and range was approximately that in Files 88, 89, and due account has been taken of such factors as the transmit and receive multipath, antenna lobe patterns, and the systematic variation of phase with decreasing range. As can be seen in the angle plot (Figure 12 B), the angle flip-flop effect has been reproduced very well, in particular, the abrupt change from predominately positive to predominately negative biases as the target passes through a receive null. In Figure 13 the simulation has been repeated with the signal modulation restored to 20 dB. (Note that the scales of these two figures are different, with the scale of Figure 13 being the same as that in Figures 4-9.)

(iv) Ground Obstacles. It is conceivable that either the direct or sea-reflected echo signal might encounter an obstacle near the radar, and that the field diffracted by the obstacle could then produce additional components to the return signal. The effects of the diffracted field would then be similar to diffuse scattering from the sea surface. Of particular concern is an old wire fence located at the verge of the cliff at a distance of 8.5 m from the receive array, which happens to be almost exactly the limit of the Fresnel zone ( $2D^2/\lambda$ ) of each dish. This fence is overgrown with an abundance of weeds and creeping vines whose weight has depressed the height of the fence from 1 m (the original vines height) to 0.3 m in certain places. The fence has a rectangular grid of 15 cm (horizontal) by 10 cm (vertical), and hence it might act as a half-infinite opaque screen, and thereby produce a diffracted ray. If we number the dishes 1, 2, 3 from bottom to top, and assume a fence height of 1 m, then the diffracted ray would enter dish 1 through the main beam near the 3 dB point of the one-way power pattern of the dish; it would enter dish 2 at a point close to the first null of the power pattern, and it would enter dish 3 at a point close to the maximum of the first sidelobe. Hence, it is conceivable that the effects of the diffracted ray could be sufficiently strong to produce the observed effects of an extra component.

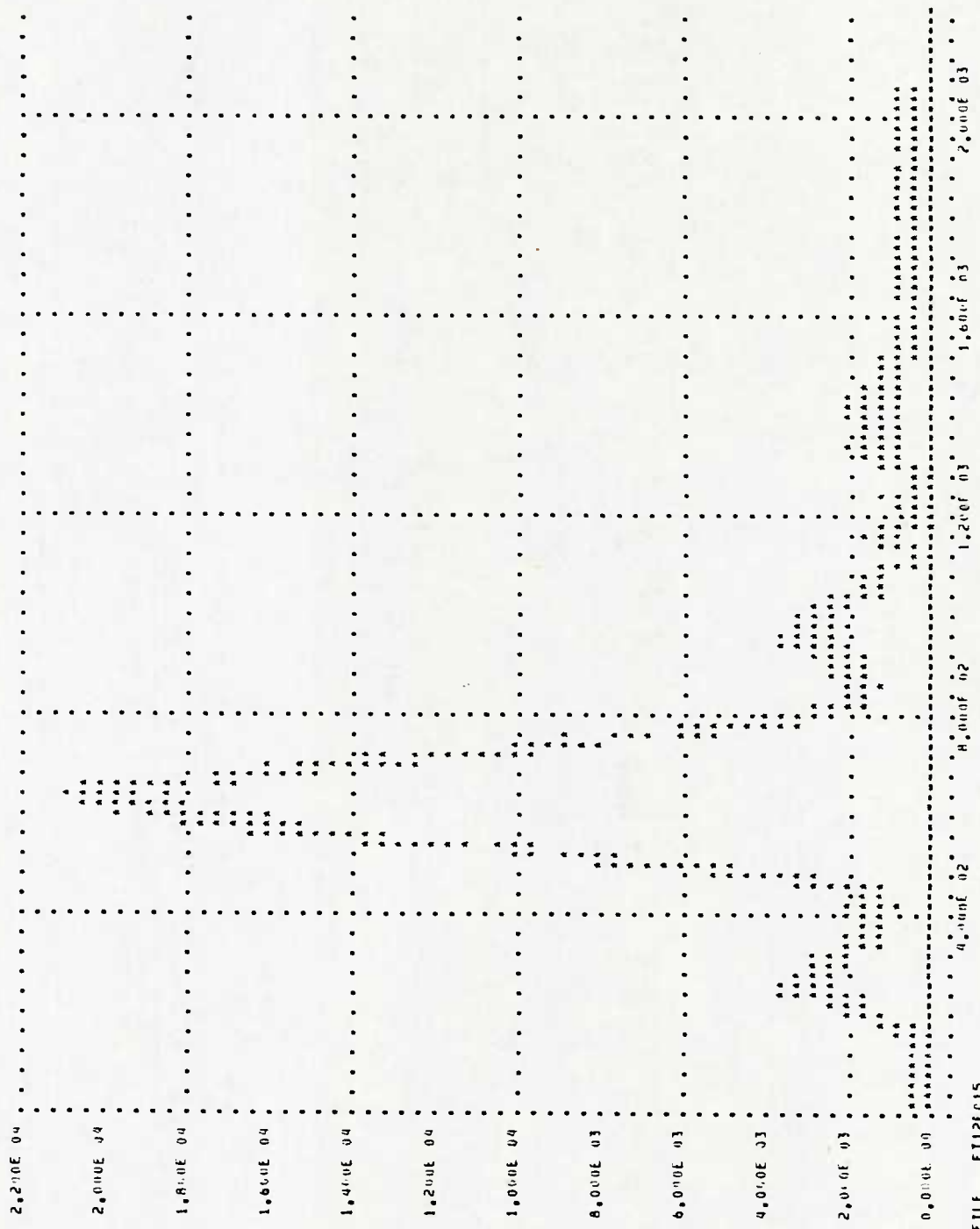
#### 4. SUMMARY, CONCLUSIONS, AND RECOMMENDATIONS

The system stability proved to be more than adequate to permit inter-channel gain and phase calibrations to be made by an appropriate numerical processing of the data. The required calibration adjustments were small, and had only small effects on the angle estimates.

The standard deviations in the elevation angle estimates were found to conform to theoretical expectations, but the biases were often larger than expected and exhibited a peculiar behavior in the vicinity of multipath receive nulls, viz., a sharp increase as the target approached a null followed by an abrupt change in sign as it emerged from the null. Refractive ray bending and uncompensated asymmetries cannot account for this "angle flip-flop" effect because they produce biases which are symmetric around the null. However, the angle flip-flop effect was reproduced in computer simulations in which a third echo component was added to the direct and specular sea-reflected rays. The additional components could have been produced either by diffuse scattering from the sea surface or by a cluttered ground environment in the near vicinity of the receive array. In particular, an old wire fence located just within the Fresnel zones of the receive dishes could have acted as a half-infinite opaque screen, and thus produce a diffracted ray which would have entered the bottom dish through its main beam, and the top dish through its first sidelobe. The angle flip-flop effect was observed on each of the three days on which the data were taken, and on each of these days the winds were extremely light so that, in terms of sea smoothness, the conditions were near optimal for simple specular reflection from the sea surface. Hence, the cluttered ground environment cannot be excluded as a possible cause for the angle flip-flop effect.

The analysis of the data was made extremely difficult by the rapid modulation on the order of 20 dB (produced by aircraft wobble and prop rotation), and if future experiments are undertaken we would recommend that a beacon be used to calibrate the system and monitor the behavior of the sea surface, and that the radar be removed to a cleaner environment.

Based on the theoretical calculations (given in [3]) it was our original goal to achieve a single pulse elevation angle estimate accuracy of approximately one-tenth of a beamwidth (0.4 degrees). If such an accuracy had been attained, the system could then be used by a surveillance radar to obtain accurate target position estimates while employed in a track while scan mode. This goal was not met since biases on the order of  $1^\circ$  were sometimes observed. (Cf. Figure 11.) However, it might be feasible to use the three subaperture method in a tracking system in which the data from many pulses is integrated as in Figure 11. The angle plots shown in Figure 11 appear to be more stable than that from a monopulse tracker, and, moreover, the phase estimates (shown in Figures 4-9) appear to be good enough to detect the presence of a multipath null. In other words, a tracker employing the three subaperture method or some similar technique could use the phase information to sense when the target is entering a region of instability, whereupon the tracker could hold its position until the phase information indicates that the target has emerged from the null, at which point the tracking algorithm would resume.



FILE FT12FC15.

Fig. 1 -- Antenna power sweep -- power (dB) vs pulse number

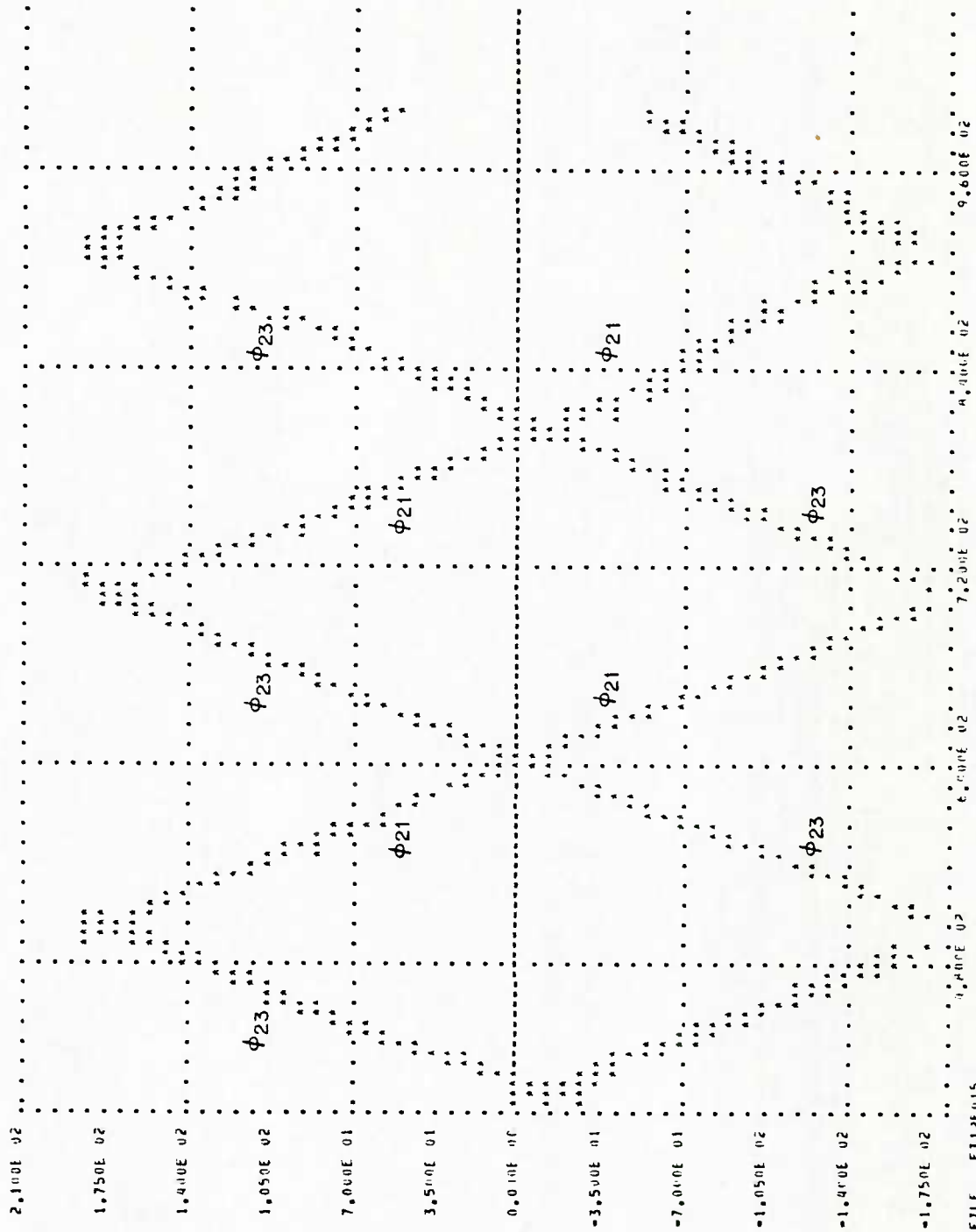


Fig. 2 — Phase sweep — phase (deg) vs pulse number

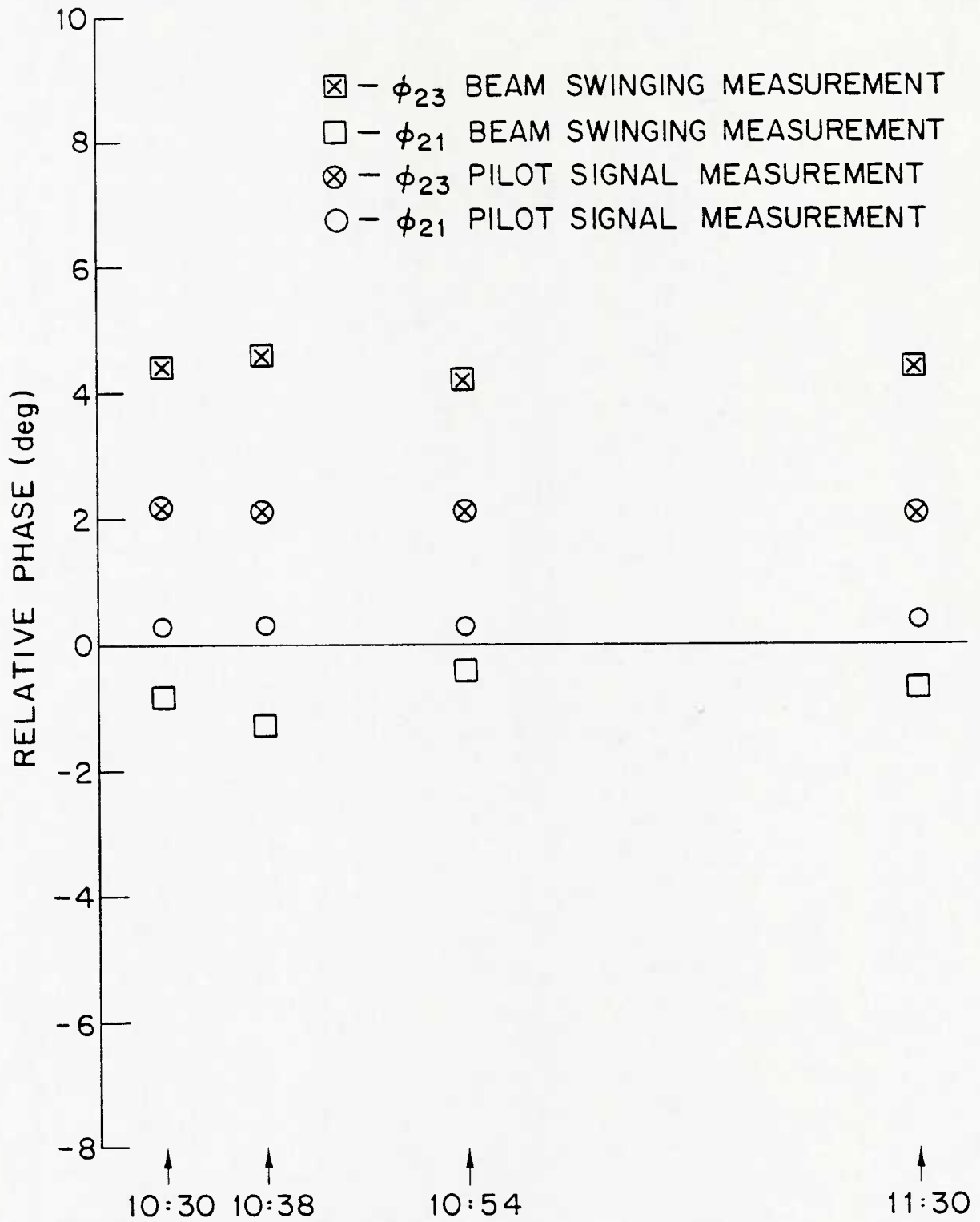


Fig. 3 - Relative phases  $\phi_{21}$ ,  $\phi_{23}$  between the center and end apertures

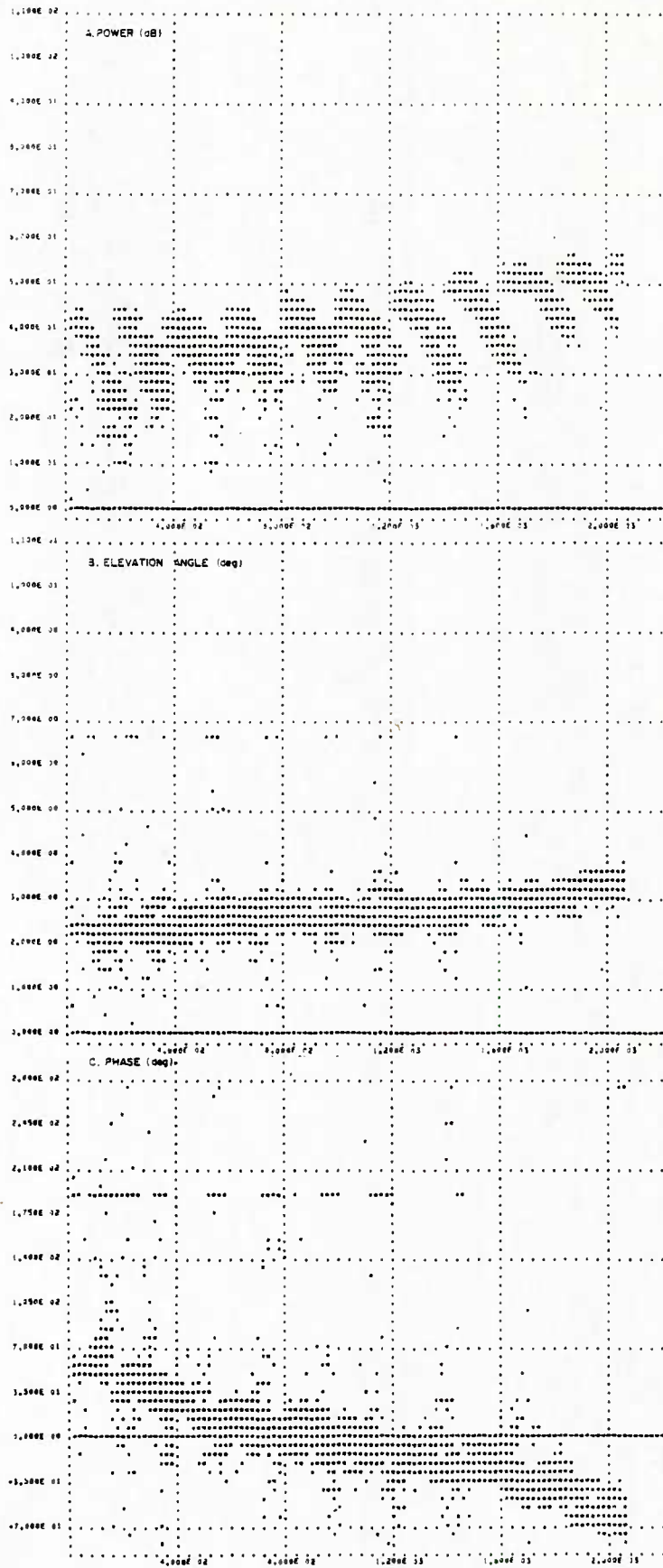


Fig. 4 - Data from File 85

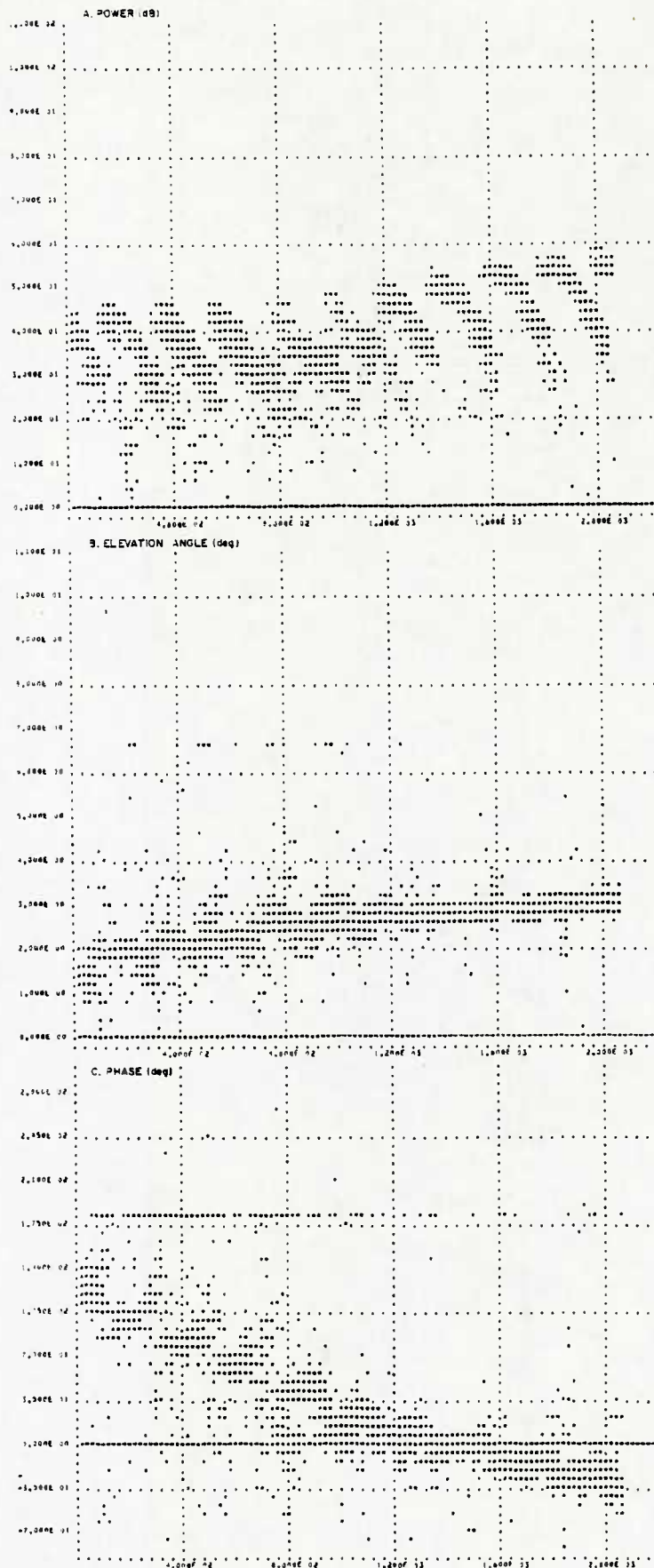


Fig. 5 — Data from File 86

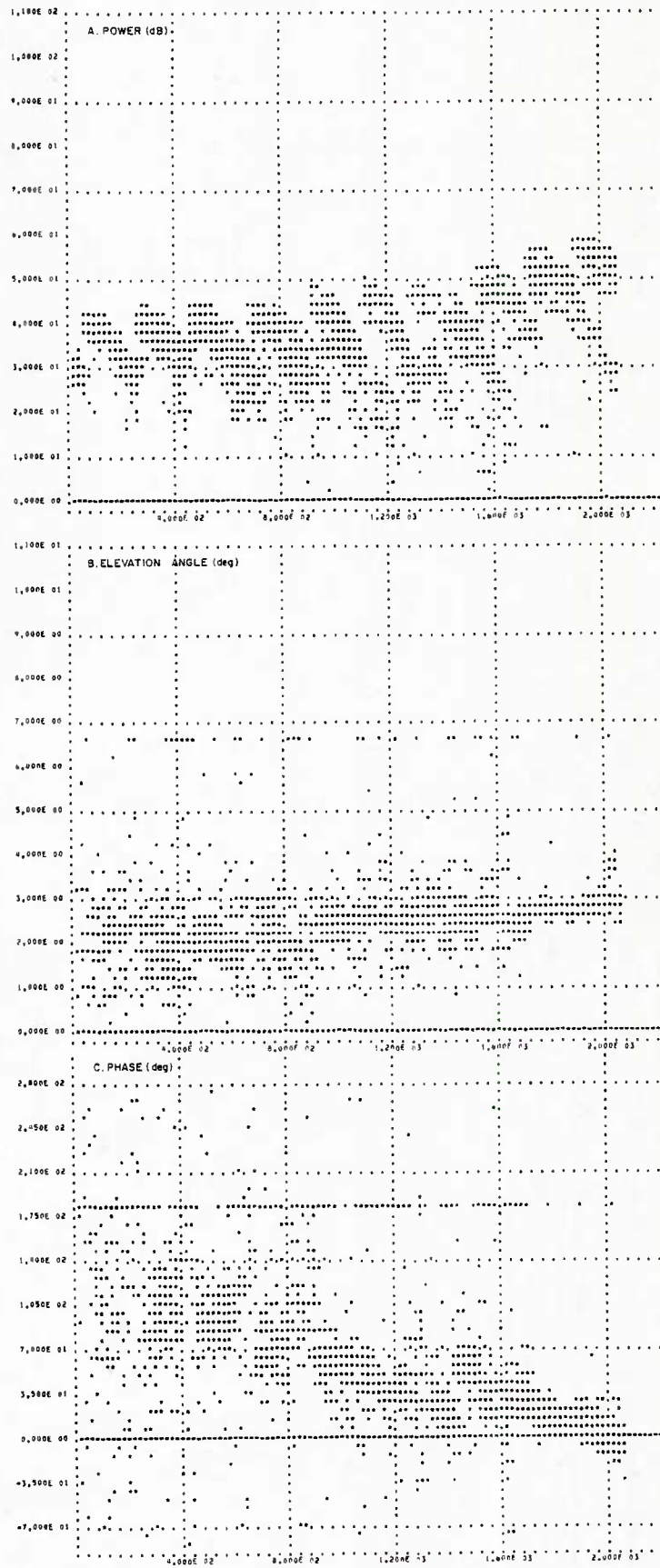


Fig. 6 — Data from File 87

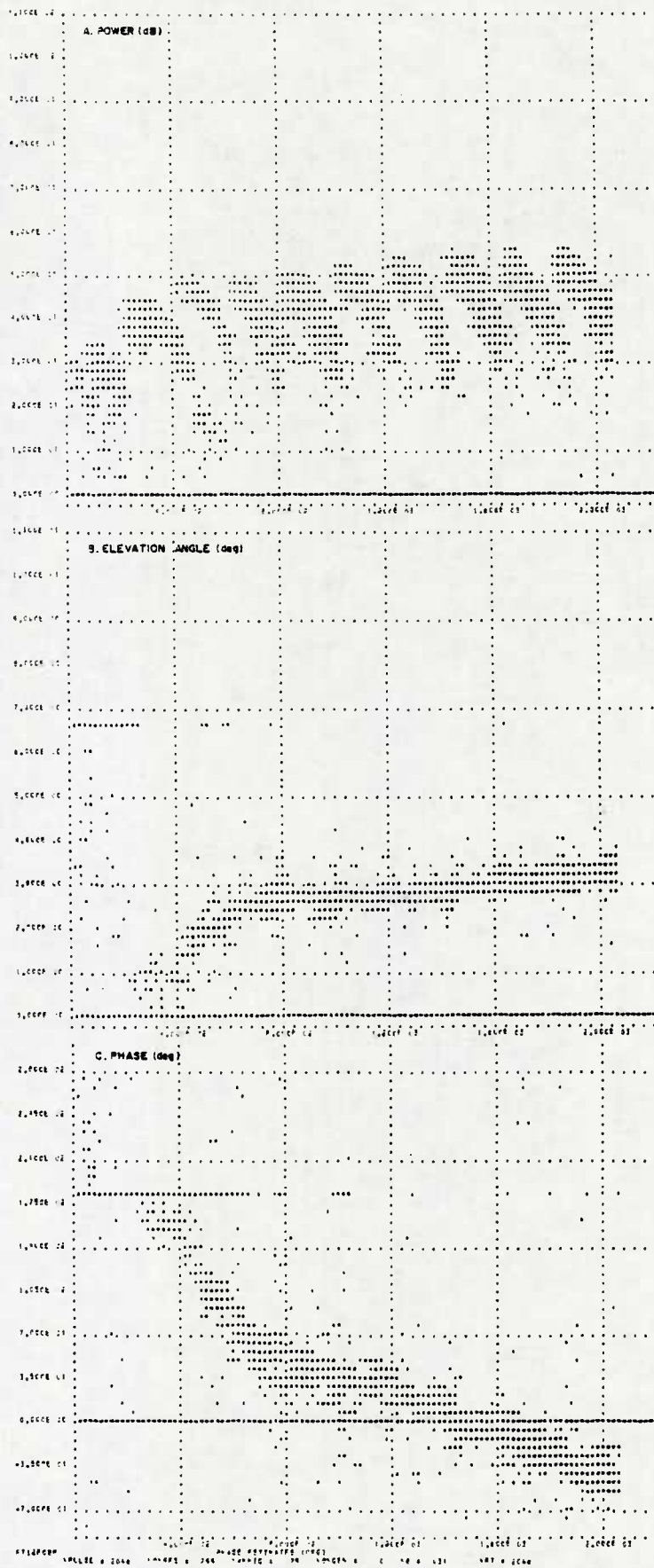


Fig. 7 — Data from File 88

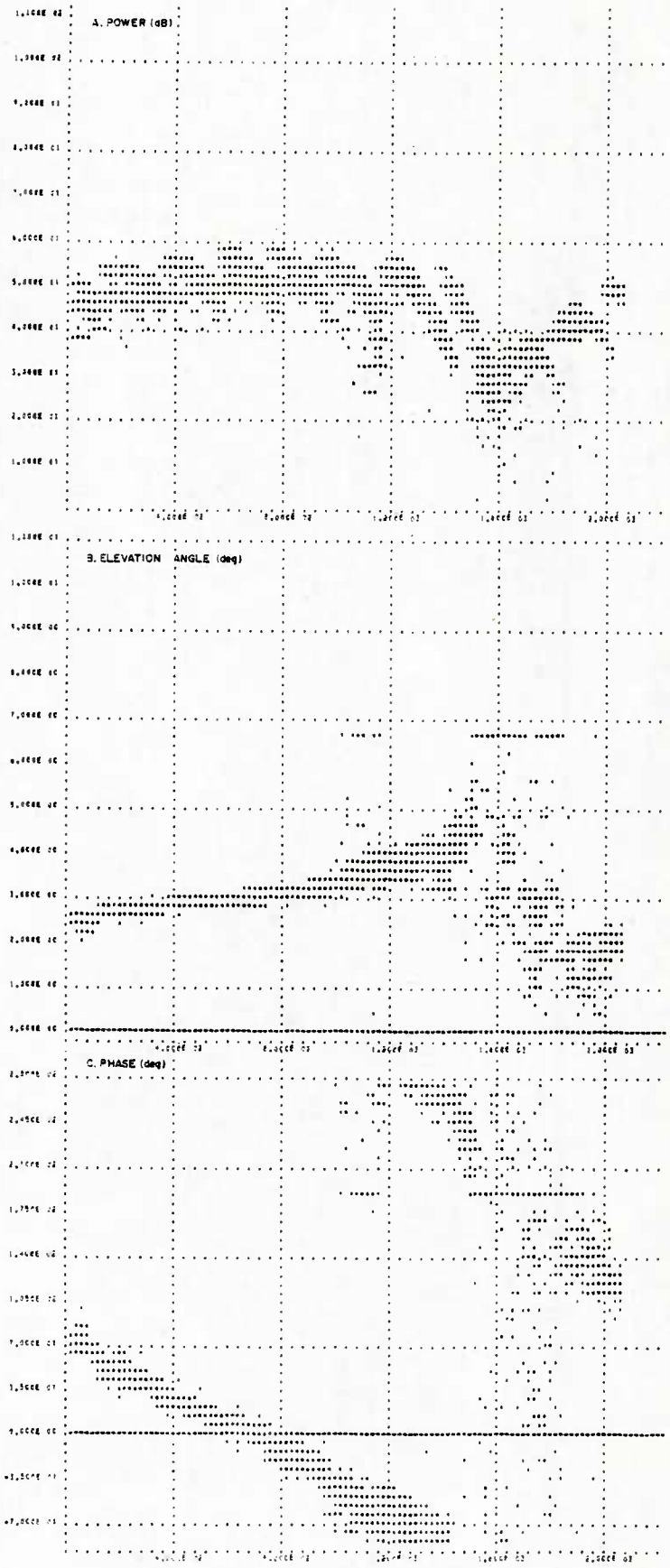


Fig. 8 — Data from File 89



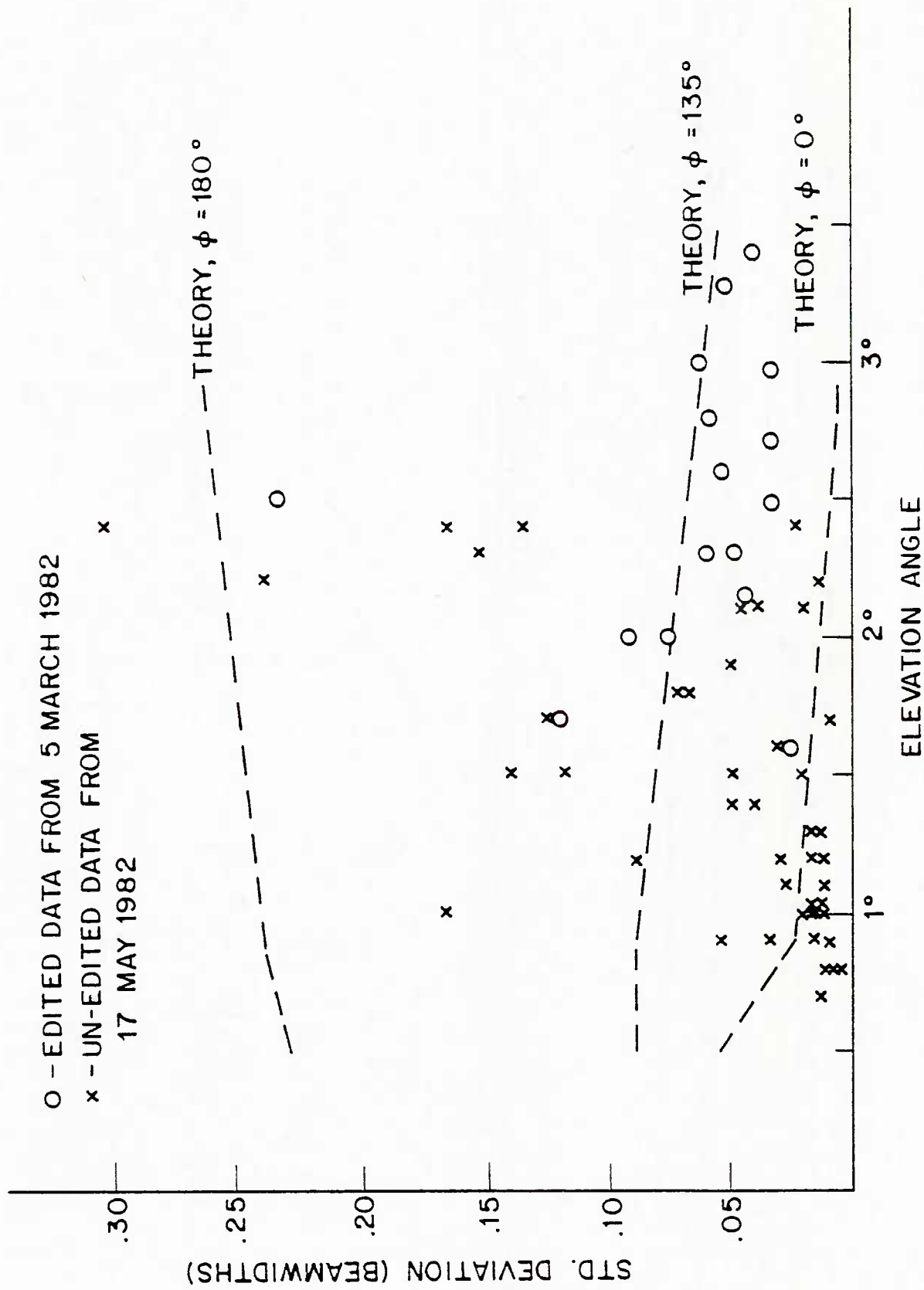


Fig. 10 - Normalized standard deviations in elevation angle measurements

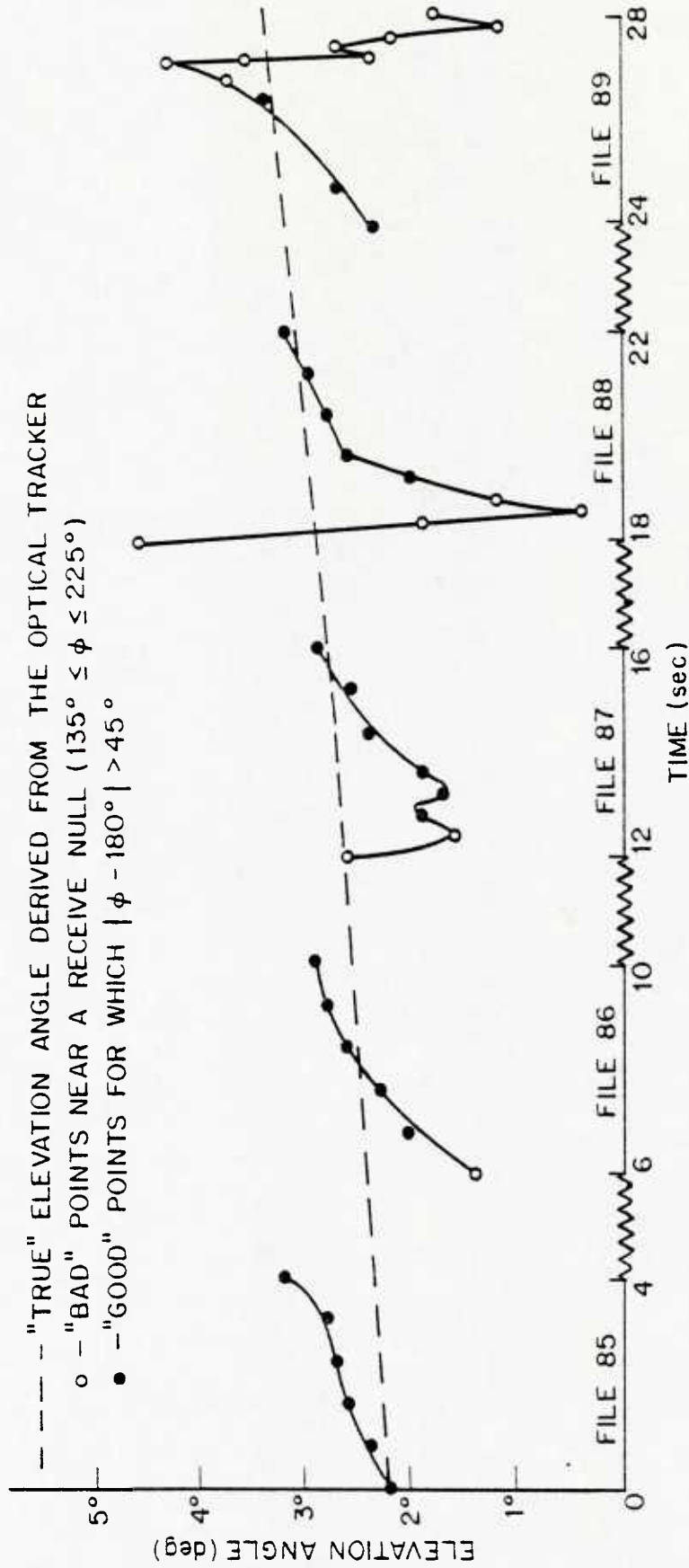


Fig. 11 — 101-Point moving average of elevation angle estimates

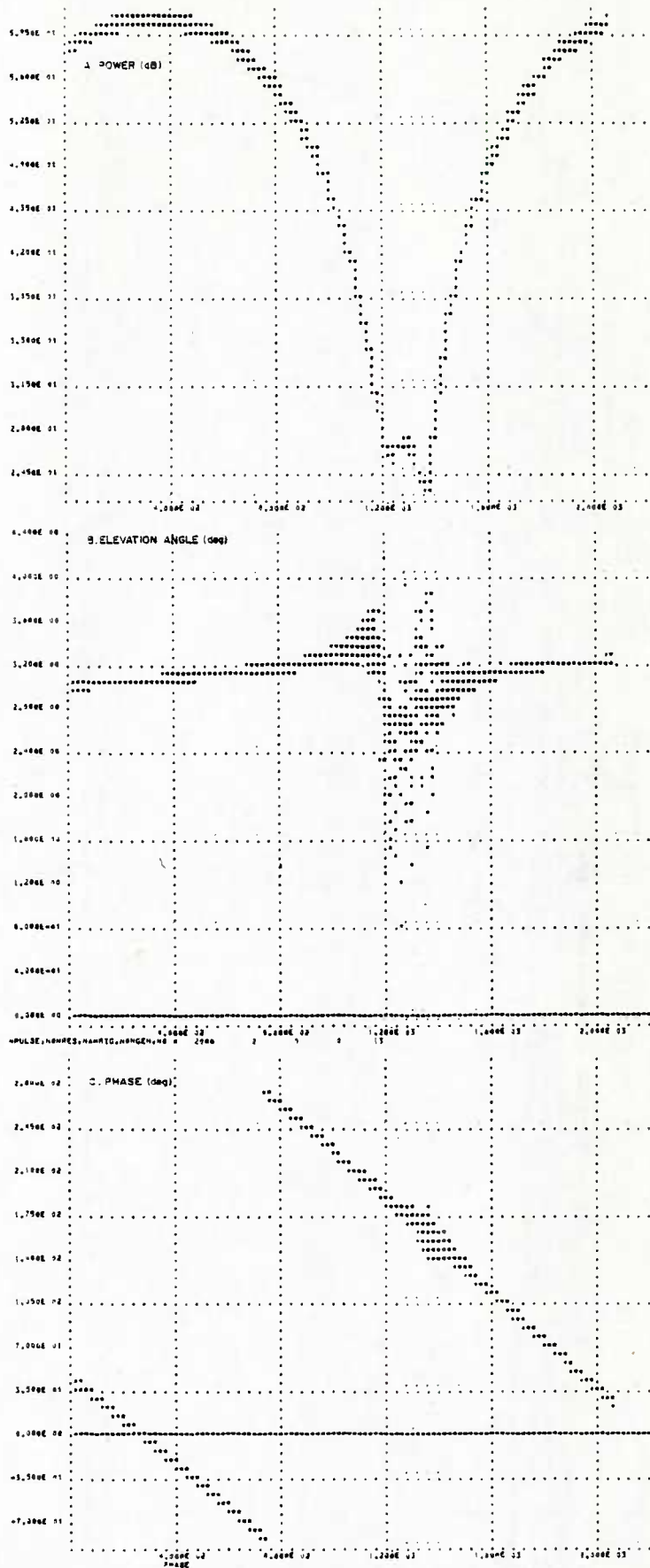


Fig. 12 — Computer simulated run with two reflected components and a 1 dB signal modulation at 15 Hz

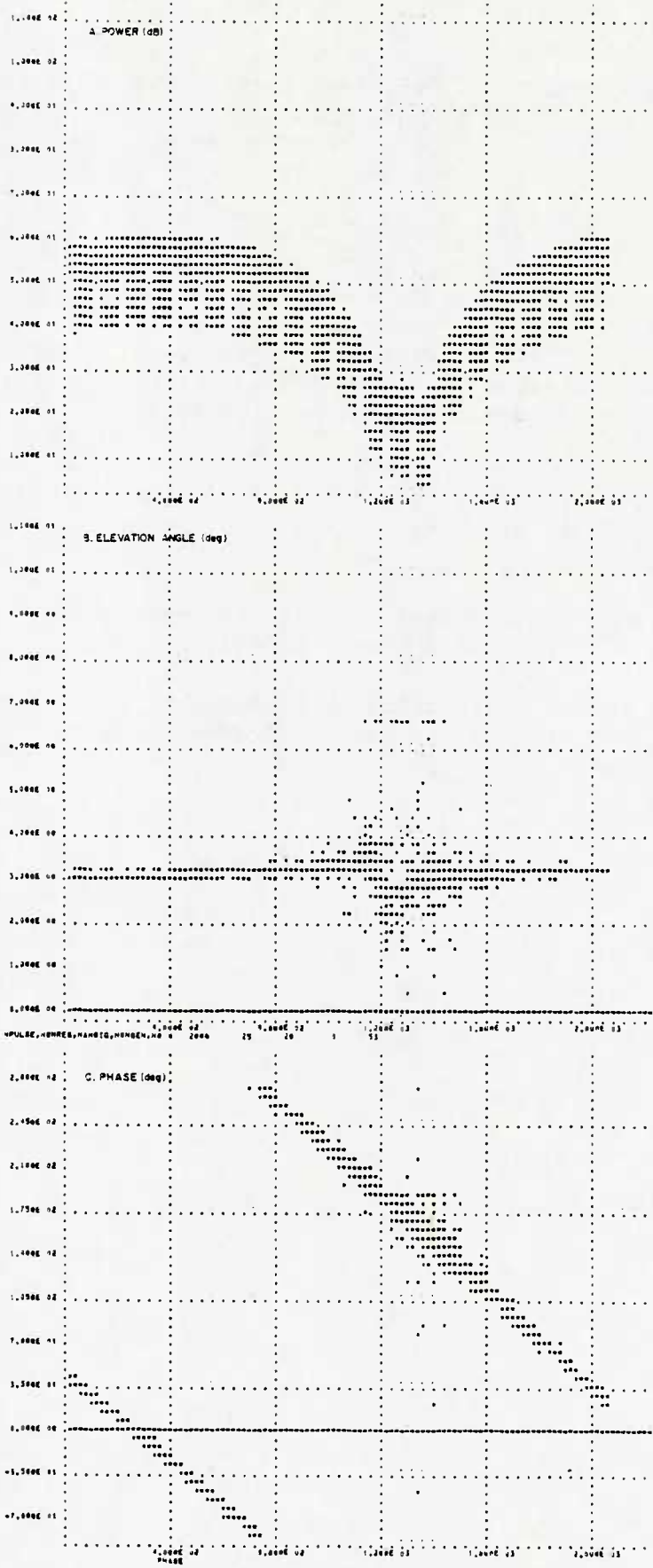


Fig. 13 — Computer simulated run with two reflected components and a 20 dB signal modulation at 15 Hz

## 5. REFERENCES

1. Trunk, G.V., Cantrell, B.H., and Gordon, W.B., "Probability density of the maximum likelihood elevation estimate of radar targets," IEEE Transactions on Aerospace and Electronic Systems, AES-15, 1 (Mar. 1979), pp. 288-290.
2. Trunk, G.V., Cantrell, B.H., and Gordon, W.B., "Bounds on elevation error estimates of a target in multipath," IEEE Transactions on Aerospace and Electronic Systems, AES-15, 6 (Nov. 1979), pp. 883-887.
3. Cantrell, B.H. Gordon, W.B., and Trunk, G.V., "Maximum likelihood elevation angle estimates of radar targets using subapertures," IEEE Transactions on Aerospace and Electronic Systems, AES-17, 2, (Mar. 1981), pp. 213-221.
4. Gordon, W.B., "Improved three subaperture method for elevation angle estimation," IEEE Transactions on Aerospace and Electronic Systems, AES-19, 1 (Jan. 1983), pp. 114-122.
5. White, W.D., "Angular spectra in radar applications," IEEE Transactions on Aerospace and Electronic Systems, AES-15, 6 (Nov. 1979), pp. 895-899.
6. Lang, S.W., "Near optimal frequency/angle of arrival estimates based on maximum entropy spectral techniques," Proc. IEEE Int. Conf. ASSP (ICASSP), pp. 829-832, Apr. 1980.

## APPENDIX A

### The Three Subaperture Algorithm

Let  $\theta_1, \theta_2$  denote the arrival angles of the target and its multipath image around the radar line-of-sight, let  $A_1, A_2$  denote their complex amplitudes, and let  $\bar{W}_1, \bar{W}_2$  be the phasors

$$W_j = \exp[2\pi i (d/\lambda) \sin \theta_j], \quad j = 1, 2 .$$

Then

$$S_n = A_1 \bar{W}_1^{(n-1)} + A_2 \bar{W}_2^{(n-1)} + \text{noise} , \quad (\text{A1})$$

where  $S_1, S_2, S_3$  are the complex receiver outputs from the three subapertures. Following [3], we set

$$\begin{aligned} \theta_1 &= \theta_B + \theta_D , \\ \theta_2 &= \theta_B - \theta_D , \end{aligned} \quad (\text{A2})$$

which can be taken as the definition of the bisector and displacement angles  $\theta_B, \theta_D$ . The corresponding phasors are denoted by  $W_B, W_D$  so that

$$\begin{aligned} W_1 &= W_B W_D , \\ W_2 &= W_B \bar{W}_D . \end{aligned}$$

At long ranges and in the absence of an array tilt (discussed in Appendix B), we have  $\theta_B = 0$  and  $W_B = 1$ . The three subaperture algorithm is the maximum likelihood estimator applied to the model (A1). After some manipulation the cost function to be minimized reduces to

$$L = \frac{|S_1 - W_B(W_D + \bar{W}_D) S_2 + W_B^2 S_3|^2}{2 + (W_D + \bar{W}_D)^2} .$$

For the results presented in this report we have used the "symmetric" form of the algorithm in which it is assumed that  $W_B$  is known, and  $L$  is minimized with respect to the variable  $W_D$  only. The variable  $W_B$  incorporates information about the asymmetries discussed in Appendix 2, and these asymmetries are "compensated" to the extent that  $\theta_B$  is accurately chosen.

There are four critical values for  $W_D$ , and the maximum likelihood solution is the critical value  $W_D$  which minimizes  $L$ . They are  $W_D = 1, W_D = -1$ , (these two being the "degenerate" solutions discussed in Section 3), and

$$W_D = (S/2) \pm i\sqrt{1-(V/2)^2}$$

where  $V$  is any root to

$$V_2 + 2 \left( \frac{2 - |R|^2}{R + \bar{R}} \right) V - 2 = 0$$

which satisfies  $|V| < 2$ , with  $R$  being given by

$$R = (S_1 + W_B^2 S_3) / (W_B S_2) \quad .$$

## APPENDIX B

### System Asymmetries

In the figure the lines HOR and LOS represent the horizon and radar line-of-sight,  $\theta_1, \theta_2$  denote the arrival angles of the target and its image around the horizon, and  $\theta_1, \theta_2$  denote the arrival angles around the line-of-sight, as in the previous appendix. As indicated in the figure,  $\theta_1, \theta_1$  are taken to be positive and  $\theta_2, \theta_2$  are negative. The (positive) angle  $\alpha$  represents the array tilt, and we have

$$\begin{aligned}\theta_1' &= \theta_1 + \alpha, \\ \theta_2' &= \theta_2 + \alpha.\end{aligned}\tag{B1}$$

The output of the algorithm is  $\theta_D$ , and we wish to show how this variable and  $\theta_B$  are related to the "true" elevation angle  $\theta_1'$ .

Let  $h$  and  $H$  denote the altitudes of the antenna and the target. Then with a little geometry we get

$$\theta_2' = -\frac{H+h}{H-h} \theta_1'\tag{B2}$$

since the image is at a distance  $H$  below the sea surface. This is the "geometric effect" discussed in Section 3.

Taking the sum of the two equations in (B1), and using (A2) and (B2) we get

$$\theta_B = -\frac{h}{H-h} \theta_1' + \alpha.$$

Similarly, taking the difference we get

$$\theta_D = \frac{H}{H-h} \theta_1'.$$

In the angle plots shown in Figures 4-9 we chose to plot  $\theta_D$  rather than  $\theta_1' = 0.9 \theta_D$  because we did not wish to disturb the position of the degenerate solutions  $\theta_D = 6.7^\circ$ . Also, much numerical work was done in experimenting with various values of the tilt  $\alpha$  in an attempt to reduce the angle flip-flop effect, but, as reported above, these were not successful.

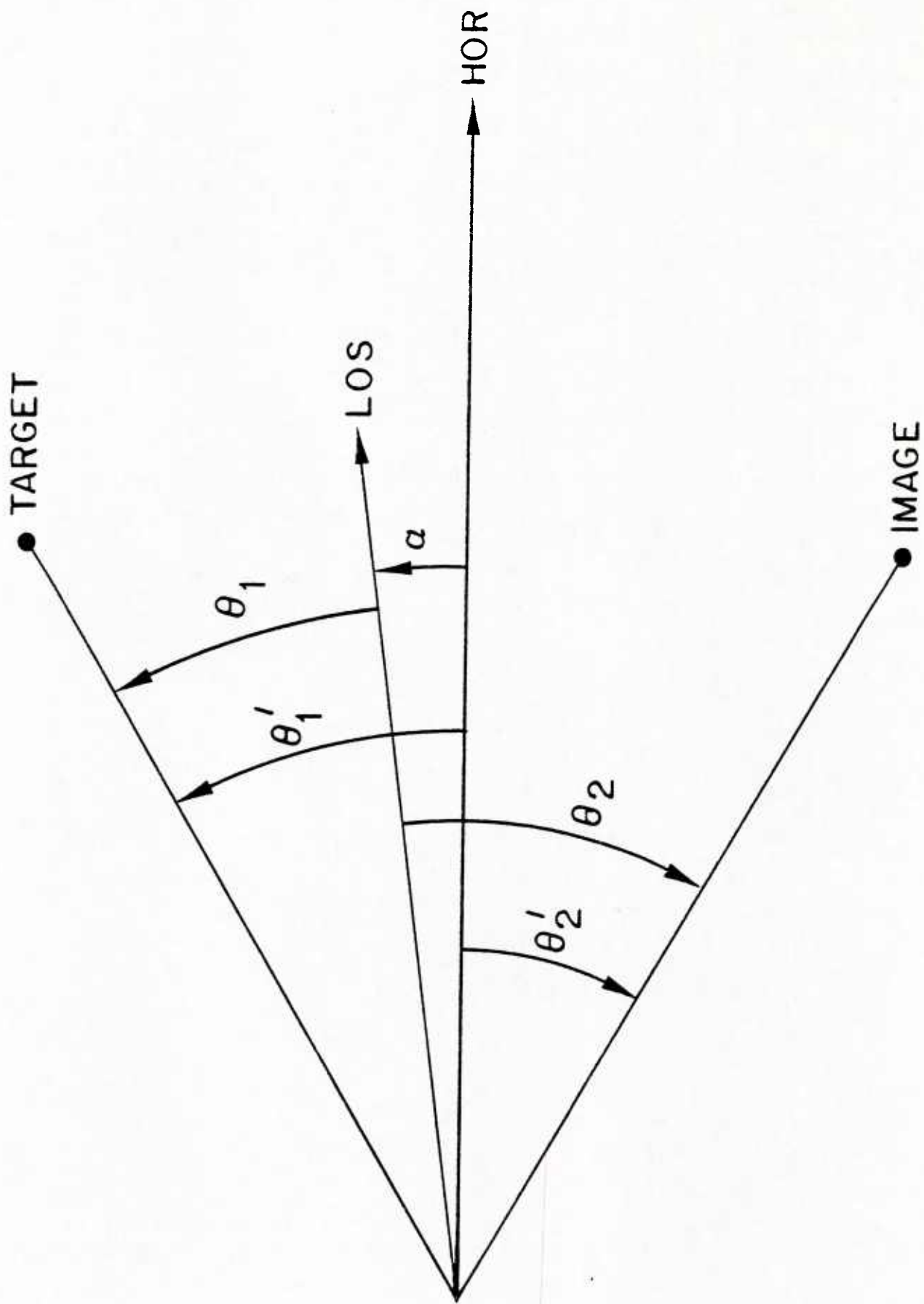


Fig. B1 — Geometry of asymmetries

U216238

DEPARTMENT OF THE NAVY

NAVAL RESEARCH LABORATORY  
Washington, D.C. 20375-5000

OFFICIAL BUSINESS  
PENALTY FOR PRIVATE USE, \$300

POSTAGE AND FEES PAID  
DEPARTMENT OF THE NAVY  
DoD-316  
THIRD CLASS MAIL

